

Suzaku X-Ray Observation of the Dwarf Nova Z Camelopardalis at the Onset of an Optical Outburst

Kei SAITOU,^{1,2} Masahiro TSUJIMOTO,¹ Ken EBISAWA,^{1,2} and Manabu ISHIDA¹

¹*Japan Aerospace Exploration Agency, Institute of Space and Astronautical Science,
 3-1-1 Yoshinodai, Chuo-ku, Sagamihara, Kanagawa 252-5210*

²*Department of Astronomy, Graduate School of Science, The University of Tokyo, 7-3-1 Hongo, Bunkyo-ku, Tokyo 113-0033
 ksaitou@astro.isas.jaxa.jp*

(Received 2011 December 2; accepted 2012 February 27)

Abstract

We present the result of a Suzaku X-ray spectroscopic observation of the dwarf nova Z Camelopardalis, which was conducted by chance at the onset of an optical outburst. We used the X-ray Imaging Spectrometer (a 38 ks exposure) and the Hard X-ray Detector (34 ks) to obtain a 0.35–40 keV spectrum simultaneously. Spectral characteristics suggest that the source was in the X-ray quiescent state despite being in the rising phase of an outburst in the optical band. The spectrum shows a clear signature of circumstellar absorption in excess of interstellar absorption and the reprocessed emission features of Fe fluorescence and Compton scattering. The extra absorption is explained due to partial coverage by either neutral or ionized matter. We found a spectral change during the observation, which is attributable only to the change in the circumstellar absorption. Such an X-ray spectral variation is reported for the first time in dwarf novae. We speculate that the variation in the circumstellar absorption is interpreted as a time-varying disk wind or geometrically flaring disk around the white dwarf during the propagation of a heat wave inward along the accretion disk at the beginning of the outburst, in which optical outburst and X-ray quiescent states co-exist.

Key words: stars: binaries: close — stars: dwarf novae — stars: individual (Z Camelopardalis) — stars: novae, cataclysmic variables — X-ray: stars

1. Introduction

Dwarf novae (DNe) are a subclass of non-magnetic cataclysmic variables, which are close binary systems consisting of a white dwarf (WD) and a late-type companion star (Warner 1995; Hellier 2001). The defining characteristic of DNe is repeated optical outbursts, in which the optical brightness increases by 2–5 mag. Thermal-viscous instability in the accretion disk is considered to be the cause (e.g., Smak 1984; Osaki 1996; Lasota 2001). The cycle repeats between two distinctive stable disk states: the quiescent state with the disk mostly made of neutral hydrogen and the outburst state mostly made of ionized hydrogen. The viscosity, surface density, and the mass accretion rate are higher in the latter state.

DNe are known to be X-ray emitters. The X-ray features typically show a dichotomy between the quiescent and outburst states. In the quiescent state, on one hand, the X-rays are from the hot and optically-thin thermal plasma, which is produced in the boundary layer between the inner edge of the accretion disk rotating at a Keplerian velocity and the WD surface rotating at a slower spin period. The plasma is localized within a height of $\sim 0.1 R_{\text{WD}}$ from the surface of the WD with a radius of R_{WD} (Mukai et al. 1997). The X-ray spectrum is very hard with a temperature beyond 10 keV and strong Fe K emission features. In the outburst state, on the other hand, the hard emission is suppressed by a factor of a few and is replaced

by extreme ultra-violet (EUV) plasma emission with a much lower temperature. This is because the plasma in the boundary layer becomes optically thicker and more efficient in radiative cooling due to the increased accretion rate to the WD.

One of the features often seen in the X-ray spectra of DNe is a complex extinction structure in the soft band (< 2 keV). The extinction cannot be explained by interstellar absorption alone, which indicates the presence of circumstellar absorption. In eclipsing systems with high inclination angles (e.g., OY Car: Ramsay et al. 2001 and V893 Sco: Mukai et al. 2009), the complex extinction can be naturally interpreted as a partial absorption by a part of the accretion disk. However, the extra extinction is also seen in some non-eclipsing systems with lower inclination angles (e.g., SS Cyg: Done & Osborne 1997 and Z Cam: Baskill et al. 2001). One idea to explain such extinction is disk wind, which is ionized to some extent and intervenes partially or fully the line of sight.

Disk winds are a phenomenon seen in any types of compact objects with an accretion disk (e.g., Ueda et al. 2001; Boirin & Parmar 2003; Kubota et al. 2007; Tombesi et al. 2010). They may play an important role in the feedback process of energy and matter from compact objects to the interstellar space and also to the intergalactic space in case of active galactic nuclei (e.g., Elvis 2006; Fabian 2010). In nearby DNe, which are accessible with optical and ultra-violet (UV) spectroscopic observations, disk

wind is observed in many systems as P Cygni profiles (Robinson 1973; Córdova & Mason 1982; Klare et al. 1982; Szkody & Mateo 1986), motivating the progress in spectral synthesis modeling of disk winds (Shlosman & Vitello 1993; Knigge et al. 1995; Feldmeier & Shlosman 1999; Long & Knigge 2002). If we can trace features of disk wind in X-ray spectra of DNe, which is yet to be established, it will bring a wider application to constrain the wind parameters in a larger number of objects in a variety of phases in the quiescent and outburst cycles. Of particular interest is the transition phase between the two states, in which we may be able to distinguish the extinction by disk wind from other causes, as we expect the disk wind to change its strength and structure during the transition.

In this paper, we present the result of a Suzaku X-ray observation of Z Cam, which was conducted by chance at the onset of an optical outburst. As we will discuss in § 5.2, the source was in the X-ray quiescent phase, despite being in the outburst phase in the optical, suggesting that the heat wave had not reached the boundary layer. We utilize this opportunity to investigate the presence of circumstellar absorption in the X-ray spectrum and examine any changes in the feature. Only a few X-ray observations were made to date in this particular phase of DN outbursts (e.g., Z Cam: Baskill et al. 2001; SS Cyg: Wheatley et al. 2003).

The plan of this paper is as follows. In § 2, we briefly summarize the basic properties of Z Cam with an emphasis on disk winds. In § 3 and § 4, we describe our observation and the result of temporal and spectral analysis, in which we present the presence of the circumstellar absorption and its time variation. We discuss some possible interpretations of our finding in § 5, and conclude in § 6.

2. Object — Z Camelopardalis

Z Cam is the archetype of the Z Cam subgroup of DNe. It is one of the brightest DNe in the optical band ($V=10.5$ – 13.0 mag) and thus is a well studied object. Major parameters are summarized in table 1.

Sources in the Z Cam subgroup show an optical outburst about every few months (~ 26 days on average for Z Cam; Oppenheimer et al. 1998). The defining characteristic of this subgroup is the “stand-still” phase after some outbursts. For a certain period of time, the brightness stays in the middle of the outburst peak and the quiescence level, rather than decaying monotonically to the quiescence level. The stand-still phase continues for several days to even years (e.g., Oppenheimer et al. 1998).

There is ample evidence that Z Cam has a mass loss in the form of wind. The object is thus used as a test bed for constructing UV spectral synthesis models of disk wind. The spatial structure of the wind is investigated by various authors (Knigge et al. 1997; Long & Knigge 2002; Hartley et al. 2005), in which rotating biconical wind was found to explain various observed features very well. It is known that the disk wind appears and disappears

depending on the phase of the outburst and quiescent cycle. The P Cygni profile of the CIV feature, which is the most prominent feature of the disk wind, was seen in the decline phase from an outburst, and one month from the start of a stand-still phase, but not in six months from the start of a stand-still and at quiescence (Szkody & Mateo 1986; Knigge et al. 1997; Hartley et al. 2005). With a poor sampling only with UV observations, a picture of the temporal behavior of the wind; i.e., when the wind starts and stops emanating from the disk, is not yet clear.

Z Cam was observed in the X-ray band several times with the EXOSAT (Mukai & Shiokawa 1993), ROSAT (Wheatley et al. 1996), and ASCA (Baskill et al. 2001) observatories. A hint of X-ray absorption by wind was seen in two ASCA observations (Baskill et al. 2001), in which extra absorption upon the interstellar absorption was required to explain the X-ray spectra. The amount of the extra absorption, which was successfully modelled by ionized absorber, was larger than the interstellar absorption by two orders of magnitude in both observations taken during an optical outburst and a transition phase from quiescence to the outburst. However, due to limited statistics and resolution in the soft energy band, a possible time variation in the circumstellar absorption was not detected between the two observations and within each observation.

3. Observation and Data Reduction

We observed Z Cam with the Suzaku satellite (Mistuda et al. 2007) on 2009 April 10. Figure 1 shows the optical light curve covering our X-ray observation taken from the American Association of Variable Star Observers (AAVSO)¹. The X-ray observation was made during the onset of an optical outburst for a total duration of 65 ks, corresponding to 2.6 orbits of Z Cam.

Suzaku has two operating instruments covering different energy ranges. One is the X-ray Imaging Spectrometer (XIS: Koyama et al. 2007) sensitive at an energy range of 0.2–12 keV. The XIS is equipped with four X-ray CCD cameras, three of which (XIS 0, 2, 3) are front-illuminated (FI) devices and the remaining one (XIS 1) is a back-illuminated (BI) device. The FI and BI devices show a superior response to each other in the hard and the soft band, respectively. The XIS 2 is dysfunctional since 2009 November, we thus used the remaining devices in this paper. In combination with four X-ray telescopes (Serlemitsos et al. 2007) co-aligned with each other, the XIS has an imaging capability to cover a 17.8×17.8 field of view (FoV) with a pixel scale of $1''.04$ pixel $^{-1}$ and a telescope half-power diameter of $\sim 2''.0$. A total effective area for the remaining three CCDs is 1030 cm 2 at 1.5 keV. The energy resolution in the full width at a half maximum (FWHM) is 170–220 eV at 5.9 keV as of the observation date.

The other instrument is the Hard X-ray Detector (HXD: Takahashi et al. 2007; Kokubun et al. 2007; Yamada et al.

¹ See <http://www.aavso.org/> for details.

Table 1. Parameters of the Z Cam system.

Parameter	Value	Unit	Method	Ref.*
Distance (d)	163^{+68}_{-38}	pc	Trigonometric parallax	[1]
Interstellar absorption ($N_{\text{H}}^{\text{ISM}}$)	4×10^{19}	cm^{-2}	UV spectroscopy	[2–5]
Inclination angle (i)	68	deg	Far-UV spectroscopy	[6]
Orbital period (P_{orb})	6.96	hour	Optical photometry and spectroscopy	[7]
WD mass (M_{WD})	0.99 ± 0.15	M_{\odot}	Radial velocity	[8]
WD radius (R_{WD})	$5.8^{+1.1}_{-1.2} \times 10^8$	cm	Mass-radius relation	[6, 9]
Companion mass (M_2)	0.70 ± 0.15	M_{\odot}	Radial velocity	[4, 8]
Companion spectral type	K7		Optical spectroscopy	[10]

* References are — [1] Thorstensen (2003); [2] Mauche et al. (1988); [3] Wheatley et al. (1996); [4] Knigge et al. (1997); [5] Baskill et al. (2001); [6] Hartley et al. (2005); [7] Thorstensen & Ringwald (1995); [8] Shafter (1983); [9] Anderson (1988); [10] Ritter & Kolb (2003).

2011) sensitive at an energy range of 10–600 keV. The HXD consists of PIN diodes and GSO scintillators, which together compose a non-imaging detector. We concentrate on the PIN data at 10–70 keV in this paper. An effective area of the PIN is $\sim 160 \text{ cm}^2$ at 20 keV. The passive fine collimators restrict the FoV to $\sim 34'$ square in the FWHM and $\sim 70'$ square in the full width at zero intensity (FWZI). The narrow FoV, the surrounding anti-coincidence detectors, and the low and stable instrumental background enable us to achieve unprecedented sensitivity in this energy band.

In our observation, the target was placed at the center of the XIS FoV. The XIS was operated in the normal clocking mode with a frame time of 8 s.

The data were screened by the standard pipeline processing version 2.3, in which we discarded events during South Atlantic Anomaly passages and Earth elevation angles below 5 degrees. For the XIS, events were further removed during the elevation angles from the sun-lit Earth below 20 degrees. For the PIN, events taken at the cut-off-rigidity of less than 6 GV were removed. As a result, we obtained a net exposure time of 38 ks for the XIS and 34 ks for the PIN. Throughout this paper, we used the HEASoft² version 6.8 for data reduction and the Xspec package version 12.7 (Arnaud 1996) for spectral fitting.

4. Analysis

4.1. Event Extraction

In the XIS image, we see no source besides Z Cam. We accumulated the source events from a circular region of 3'13 (180 pixels) in radius, which maximizes the signal-to-noise ratio. The background events were extracted from an annulus of 4'–7' radii concentric to the source region. The encircled energy fraction of the background region is approximately 3% of the source region.

For the PIN, which is a non-imaging detector, the background consists of the instrumental non-X-ray background (NXB), the cosmic X-ray background (CXB), and possible contaminating sources within the FoV. We used NXB events provided by the instrument team (Fukazawa et al.

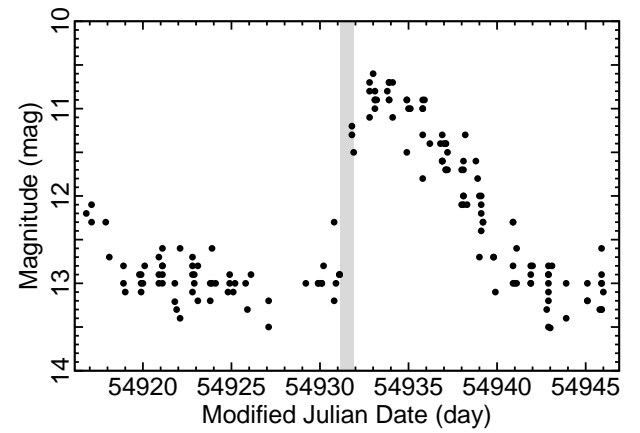


Fig. 1. Optical light curve of Z Cam taken from the AAVSO. The duration of the Suzaku observation is represented by the shaded region.

2009) and simulated CXB events assuming a model obtained with the HEAO-1 satellite (Boldt 1987). We checked the latest INTEGRAL IBIS (Bird et al. 2010) and Swift BAT (Cusumano et al. 2010) catalogues and found no contaminating source within the FWZI FoV of the PIN.

4.2. Temporal Analysis

Using the XIS (0.2–12 keV) and PIN (14–40 keV) data, we constructed light curves of the background-subtracted count rate (figure 2). We constructed the curves with several different time bins to find any changes in a wide range of time scales. As a result, we found two apparent changes of different time scales.

One is a fluctuation in the XIS count rate in a short time scale of ~ 100 s, which was found most prominently in the light curve binned with 16 s. The count rate changes by $\sim 50\%$ in a range of $2\text{--}8 \text{ s}^{-1}$ with a mean of 4.1 s^{-1} in this bin size.

The other is an increase in the XIS count rate at around the $\sim 30\text{--}50$ ks interval from the start of the observation (figure 2a). In order to investigate this change further, we also constructed band-limited curves in the soft (0.2–2 keV) and the hard (2–12 keV) band of the XIS (figure 2b

² See <http://heasarc.nasa.gov/docs/software/lheasoft/> for details.

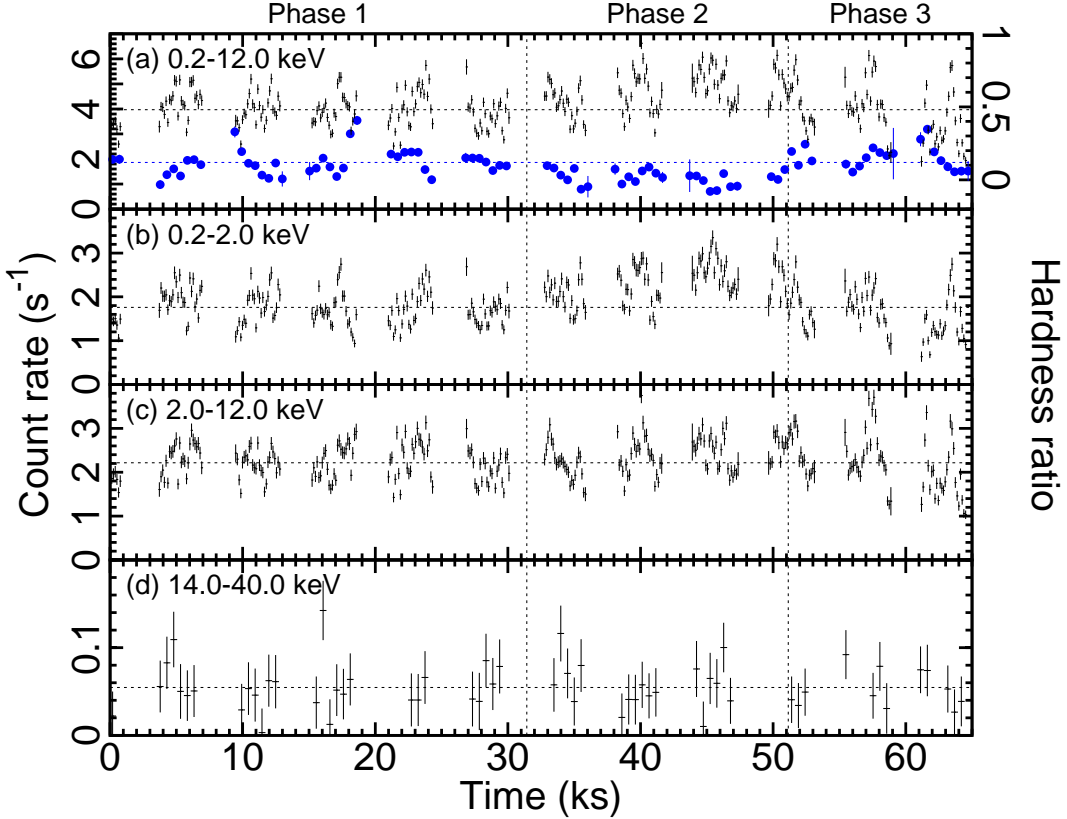


Fig. 2. Light curves of background-subtracted count rates in the (a) 0.2–12 keV, (b) 0.2–2.0 keV, and (c) 2.0–12.0 keV bands using the XIS and (d) 14–40 keV band using the PIN. The light curve of the hardness ratio in the XIS band is overlaid in (a). The curves are binned with 128 s for the XIS count rate curves, 512 s for the PIN count rate curve and the XIS hardness ratio curve. The discontinuities are due to Earth occultation of the object. A 1σ Poisson statistical uncertainty is given. The three phases are divided by the dotted vertical lines. The dotted horizontal lines indicate the mean count rate and the mean hardness ratio derived from phase 1. The origin of the abscissa is the time of the observation start at MJD= 54931.147 d.

and c, respectively), as well as the hardness ratio (figure 2a; blue curve) defined as $(H + S)/(H - S)$, where H and S are the count rate in the hard and the soft band, respectively. The change in the ~ 30 – 50 ks interval is significantly seen only in the soft band, which is confirmed both with the count rate and the hardness ratio curves. No similar change is seen in the PIN light curve (figure 2d). For time-sliced spectroscopy in later sections (§ 4.4), we divided the observation time into three phases; phase 2 being the interval with a significant decrease in the hardness ratio and the phases 1 and 3 being the intervals prior and posterior to the phase 2, respectively (figure 2).

We also investigated changes associated with the orbital period of $P_{\text{orb}} = 25.0$ ks. Figure 3 shows a count rate curve folded by the period, in which no apparent variation was found except for the short time fluctuation seen also in the light curve before folding (figure 2). To quantify the claim, we compared the mean count rate and its standard deviation between the folded and unfolded curves and found that they are consistent with each other. In fact, similar fluctuation was seen in light curves folded by any other arbitrary chosen periods. Also, the aforementioned feature of the hardness change in the 30–50 ks interval was seen only once and did not repeat itself. We thus conclude

that there is no X-ray change associated with the orbital period.

4.3. Spectral Analysis (1): Time-Averaged Spectrum

We first present the spectral fitting for the time-averaged spectrum. We constructed background-subtracted spectrum using the XIS and the PIN. For the XIS, we generated the detector and telescope response files using the `xisrmfgen` and `xissimarfgen` (Ishisaki et al. 2007) tools, respectively. The two FI spectra were merged for their nearly identical response, while the BI spectrum was treated separately. The 1.8–2.0 keV band was removed for a known calibration uncertainty at the Si K edge. At the soft-band end of the response, which is affected by accumulating contamination material on the surface of the CCDs, the calibration has shown some progress recently by introducing time variability in the chemical composition of the contaminants. We examined the spectra of two calibration sources, 1E 0102.2–7219 and RX J1856.5–3754, that are closest in time with ours and found that the systematic uncertainty in the lowest end of the response is $\lesssim 20\%$ at 0.35 keV from the deviation of the response-convolved model to the data. For the PIN, we used the standard detector response file distributed by

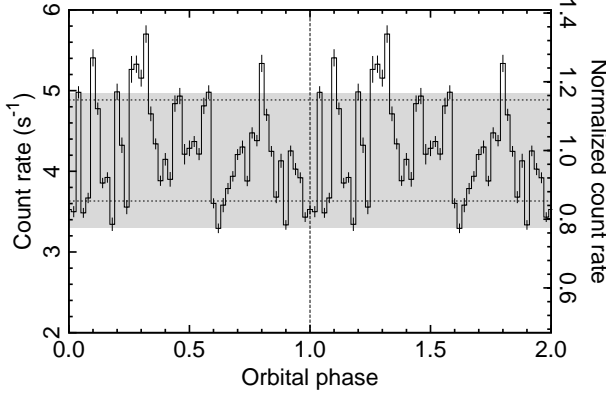


Fig. 3. Light curve folded by the orbital period in 0.2–12 keV with a bin size of ~ 500 s bin^{-1} . A 1σ Poisson statistical uncertainty is given for the data. Two orbital phases are shown for clarity. The orbital phase 0.0 corresponds to the observation start. The vertical ticks on the left-hand side represent the count rate, while those on the right-hand side represent the count rate normalized by the mean count rate. The standard deviation of the count rate is shown with the horizontal dotted lines for the folded light curve and with the gray bands for the unfolded light curve.

the instrument team.

Figure 4 shows the 0.35–40 keV spectrum using both the XIS and the PIN. The most prominent feature in the entire spectrum is the intense emission lines at 6.7 and 7.0 keV respectively from the $n = 2 \rightarrow 1$ lines by Fe XXV and the Ly α line by Fe XXVI, which indicates an optically-thin thermal plasma. Other features can also be noticed.

In order to characterize the spectrum, we began with a simple model; i.e., multi-temperature thin-thermal plasma model (`cemeek1`) attenuated by photoelectric absorption (`tbabs`: Wilms et al. 2000) of a column fixed to the interstellar value (table 1). The multi-temperature model is an integral of a single-temperature plasma model (`mekal`: Mewe et al. 1985; Mewe et al. 1986; Kaastra 1992; Liedahl et al. 1995) with a differential emission measure (EM) as a function of the plasma temperature (T) in a power-law form of $d(EM)/dT \propto (T/T_{\max})^{\alpha-1}$. Such a model is widely used to describe X-ray spectra from CVs (e.g., Done & Osborne 1997; Baskill et al. 2005). The free parameters were the maximum temperature (T_{\max}) and the power (α) in the distribution as well as the abundance (Z) changed collectively for all metals relative to hydrogen with respect to the solar value. We employed the solar abundance by Wilms et al. (2000) and the photoionization cross-sections by Verner et al. (1996). The 4–10 keV data were used for the fitting, and the best-fit model was extrapolated both to the lower and upper energy ranges (figure 4). We multiplied a constant of 1.164 to the PIN normalization against the XIS to compensate for the known systematic difference between the two³. We call this model a “fiducial model”.

The residuals to the fiducial model (figure 4) indicate

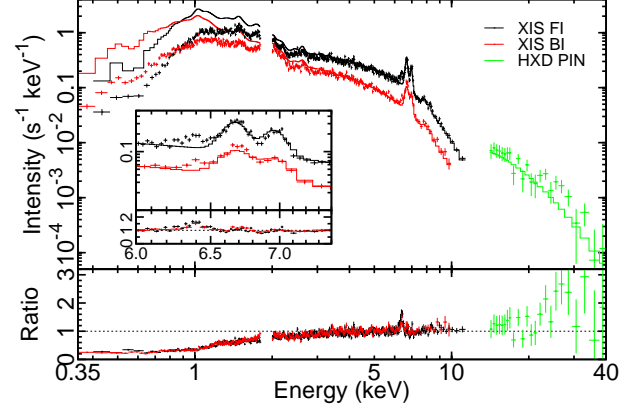


Fig. 4. Background-subtracted and time-averaged spectrum fitted intentionally with a simple model of multi-temperature thin-thermal plasma emission attenuated by the absorption fixed to the interstellar value. The 4–10 keV data were used for the fitting. The data (crosses) and the best-fit model (solid lines) are shown in the upper panel, while the ratio of the data to the best-fit model is in the lower panel. An enlarged view at the Fe K α complex band is shown in the inset.

that the spectral model requires other components to account for the following: (1) excess emission line at 6.4 keV presumably from Fe I K α fluorescent emission, (2) extra attenuation below ~ 2 keV, which is attributable to extinction by circumstellar medium (CSM), and (3) excess emission above ~ 20 keV, which is a signature of Compton-scattered continuum emission. In the given spectrum, we found that these multiple spectral components are coupled with each other. Therefore, we started by inspecting each component separately by local fitting in carefully selected energy bands (§ 4.3.1–§ 4.3.3) and then conducted the entire fitting with a synthesized model (§ 4.3.4).

4.3.1. Fe fluorescent line

First, we constrained the emission line at 6.4 keV. We fitted the 4–10 keV spectrum with the fiducial model plus a Gaussian line component. The center energy and the intensity of the line were the free parameters, while the intrinsic width was fixed to 0 eV in the fitting. We obtained the best-fit center energy of $6.40^{+0.02}_{-0.01}$ keV, which is consistent with the K α fluorescence line from Fe I. We fixed the center energy to this value in the following steps.

4.3.2. Reflection component

Second, we constrained the excess continuum emission by Compton scattering in the PIN band. The fluorescence and the Compton scattering are coupled physically under the same geometry with a common parameter $\Omega/2\pi$; the solid angle subtended by the reflector viewed from the plasma (figure 5). However, because no spectral model is available to account for both processes in `Xspec`, we iterated the fitting procedure until we obtained a converged result between the two. The relation between the equivalent width (EW_{FeI}) of the Fe fluorescence line and the viewing angle ($\Omega/2\pi$) was taken from George & Fabian (1991). The inclination angle was fixed to the value in table 1.

We fitted the 4–40 keV spectrum using the fiducial

³ See a Suzaku memo (<http://www.astro.isas.jaxa.jp/suzaku/doc/suzakumemo/suzakumemo-2008-06.pdf>) for details.

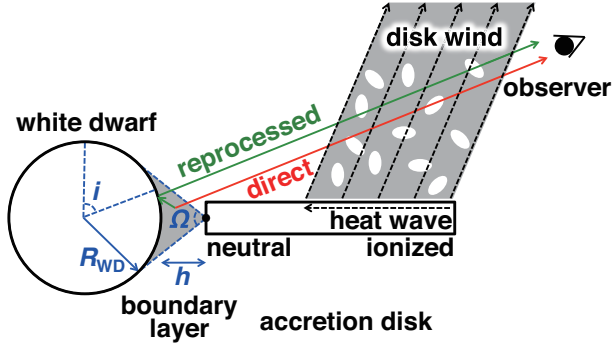


Fig. 5. Schematic view of the plasma structure and the disk wind. The disk wind is illustrated for only the upper-right part of the accretion disk.

model plus a Gaussian line component, which is modified by the Compton reflection model (`reflect`: Magdziarz & Zdziarski 1995). We started with $\Omega/2\pi = 1$ as an input parameter for the Compton reflection model. The derived EW_{FeI} was compared with the value expected to constrain the viewing angle $\Omega/2\pi$. In George & Fabian (1991), a power-law spectrum is assumed for the photo-ionization continuum emission. We approximated the best-fit thermal model with a power-law model in the 7.11–10 keV band, and derived the power-law slope. We also corrected for the Fe abundance [Fe/H]; we used 2.69×10^{-5} , while George & Fabian (1991) assumed 3.3×10^{-5} . The derived $\Omega/2\pi$ value was used as an input parameter of the Compton reflection model in the next iteration. This process was repeated until we obtained a converged value of $\Omega/2\pi = 0.484$. The parameter is fixed to this value in the following steps.

4.3.3. Additional absorber

Third, we constrained the additional extinction prominent below ~ 2 keV (figure 4). We convolved the model described above with several additional absorption models and compared their reduced χ^2 values (χ^2_{red}) in the 0.35–1.8 keV band (figure 6).

For the additional model, we started with the photoelectric absorption by neutral matter using the same model with the interstellar absorption (`tbabs`). This model was unsuccessful with $\chi^2_{\text{red}} = 1.90$ for 309 degrees of freedom (dof).

The residual (figure 6b) indicates that the observed spectrum remains less attenuated than the model predicts despite the fact that the deviation from the fiducial model (figures 4 and 6a) starts at an energy as high as ~ 3 keV. This is a signature of either or both of the partial coverage by the absorber or the absorber being ionized. We thus employed a partial absorption by neutral matter (`pcfabs`), a full absorption by ionized matter (`zxipcf` with the covering fraction fixed to 1), or a partial absorption by ionized matter (`zxipcf`, in which the covering fraction is a free parameter). The `zxipcf` model is calculated using the `XSTAR` code (Bautista & Kallman 2001). The free parameters in the `pcfabs` model are the absorption column ($N_{\text{H}}^{\text{CSM}}$) and the covering fraction (C^{CSM}), while those

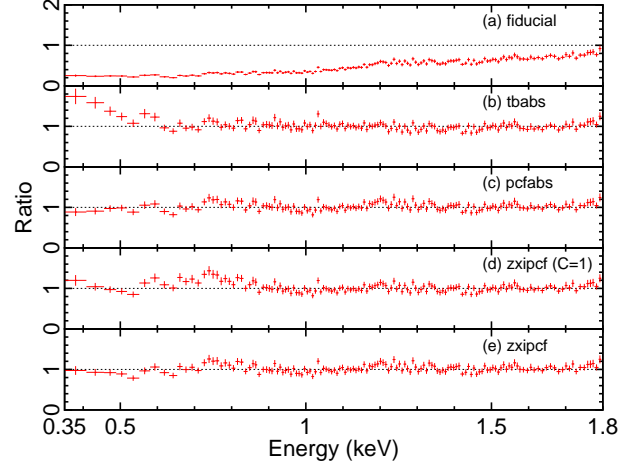


Fig. 6. Ratio of the data against the models with different circumstellar absorption models: (a) the fiducial model (no absorption by CSM), (b) the `tbabs` model, (c) the `pcfabs` model, (d) the `zxipcf` model with the covering fraction $C^{\text{CSM}} = 1$, and (e) the `zxipcf` model. The BI spectrum is displayed.

of the `zxipcf` are $N_{\text{H}}^{\text{CSM}}$, C^{CSM} , and the ionization parameter (ξ^{CSM}). There is a systematic deviation in the residual around 0.7–0.8 keV for the full-covering ionized model (figure 6d), while no such deviation is seen in the entire soft-band spectrum for the partial-covering neutral and ionized models (figure 6c and e). Indeed, the latter two show a better χ^2_{red} values of 1.46 (dof = 308) and 1.47 (dof = 307), respectively, than the former of 1.79 (dof = 308). We therefore used partially-covering neutral or ionized matter for the additional absorption in the following steps.

4.3.4. Entire fitting

Finally, we combined all the aforementioned components to fit the entire spectrum in the 0.35–40 keV band. To the fiducial model, we added a Gaussian line and convolved with the Compton reflection model and one of the two additional absorption models: partial absorption by neutral or ionized matter. We conducted the iteration process described in § 4.3.2 to reach a consistent geometrical solution between the fluorescence and the Compton scattering. We obtained a successful fit for the two models of the additional absorption, which are shown in figure 7 and tables 2 and 3.

4.4. Spectral Analysis (2): Time-Sliced Spectra

We now proceed to time-sliced spectroscopy. Figure 8 shows the BI spectra in the three phases defined in figure 2. The elevated count rate in phase 2 in the soft band (0.2–2.0 keV) is confirmed in the time-sliced spectra. We applied the model constructed for the time-averaged spectra to the spectra of all slices. The best-fit parameters are shown in tables 2 and 3.

The result of the fitting indicates that the time variation in phase 2 is attributable only to a change in the circumstellar absorption; other parameters do not change among the slices. Figure 9 shows the contour plots of the

Table 2. Best-fit parameters for the neutral partial covering absorption model.*

Phase	$N_{\text{H}}^{\text{ISM}}/10^{21}$ (cm $^{-2}$)	$N_{\text{H}}^{\text{CSM}}/10^{21}$ (cm $^{-2}$)	C^{CSM}	$\Omega/2\pi$	α	kT_{max} (keV)	Z^{\dagger} (Z_{\odot})	EW_{FeI} (eV)	χ^2_{red} (dof)
Averaged	0.04 ‡	$8.9^{+0.5}_{-0.6}$	$0.75^{+0.002}_{-0.02}$	0.484 ‡	$1.00^{+0.07}_{-0.07}$	$21.0^{+1.3}_{-1.2}$	$2.10^{+0.11}_{-0.10}$	65^{+9}_{-9}	1.32 (860)
Phase 1	0.04 ‡	$8.8^{+0.8}_{-0.8}$	$0.80^{+0.02}_{-0.02}$	0.484 ‡	$0.97^{+0.11}_{-0.12}$	$22.3^{+1.9}_{-1.7}$	$2.04^{+0.16}_{-0.15}$	63^{+14}_{-13}	1.28 (617)
Phase 2	0.04 ‡	$7.1^{+1.1}_{-1.2}$	$0.61^{+0.03}_{-0.04}$	0.484 ‡	$1.15^{+0.12}_{-0.12}$	$18.7^{+1.8}_{-1.2}$	$1.99^{+0.18}_{-0.16}$	52^{+16}_{-18}	1.06 (486)
Phase 3	0.04 ‡	$11.2^{+1.0}_{-1.0}$	$0.83^{+0.03}_{-0.03}$	0.484 ‡	$0.84^{+0.13}_{-0.13}$	$23.5^{+3.4}_{-2.2}$	$2.43^{+0.25}_{-0.23}$	91^{+21}_{-19}	1.25 (331)

* The parameters are the hydrogen column density of the interstellar medium ($N_{\text{H}}^{\text{ISM}}$) and that of the additional absorber ($N_{\text{H}}^{\text{CSM}}$), the covering fraction (C^{CSM}), the solid angle of the cold reflector viewed from the plasma ($\Omega/2\pi$), the power-law index of the emission measure (α), the maximum temperature of the plasma (kT_{max}), the abundance of the plasma (Z), the equivalent width of 6.4 keV line (EW_{FeI}), and the reduced χ squared (χ^2_{red}), and the degree of freedom (dof). The errors indicate the 90% statistical uncertainty.

† We note that the abundance values are mainly determined from the iron lines, which are the most prominent lines, and an abundance of $Z_{\text{Fe}} = 2.0$ in Wilms et al. (2000) ($[\text{Fe}/\text{H}] = 2.69 \times 10^{-5}$) is equivalent to that of ~ 1.1 in Anders & Grevesse (1989) ($[\text{Fe}/\text{H}] = 4.68 \times 10^{-5}$).

‡ The values are fixed.

Table 3. Best-fit parameters for the ionized partial covering absorption model.*

Phase	$N_{\text{H}}^{\text{ISM}}/10^{21}$ (cm $^{-2}$)	$N_{\text{H}}^{\text{CSM}}/10^{21}$ (cm $^{-2}$)	C^{CSM}	ξ^{CSM} (erg s $^{-1}$ cm)	$\Omega/2\pi$	α	kT_{max} (keV)	Z^{\dagger} (Z_{\odot})	EW_{FeI} (eV)	χ^2_{red} (dof)
Averaged	0.04 ‡	$5.3^{+0.5}_{-0.7}$	$0.82^{+0.02}_{-0.02}$	$-0.62^{+0.08}_{-0.15}$	0.484 ‡	$1.02^{+0.06}_{-0.06}$	$18.6^{+0.7}_{-0.4}$	$1.93^{+0.10}_{-0.09}$	62^{+8}_{-9}	1.31 (859)
Phase 1	0.04 ‡	$5.5^{+0.4}_{-1.4}$	$0.88^{+0.02}_{-0.02}$	$-0.55^{+0.02}_{-0.31}$	0.484 ‡	$0.98^{+0.08}_{-0.12}$	$20.0^{+1.8}_{-1.5}$	$1.90^{+0.18}_{-0.16}$	60^{+13}_{-15}	1.29 (616)
Phase 2	0.04 ‡	$4.3^{+0.6}_{-2.3}$	$0.69^{+0.04}_{-0.04}$	$-0.59^{+0.11}_{-0.82}$	0.484 ‡	$1.10^{+0.11}_{-0.10}$	$18.6^{+1.8}_{-1.4}$	$1.93^{+0.18}_{-0.17}$	50^{+16}_{-16}	1.06 (485)
Phase 3	0.04 ‡	$6.0^{+1.3}_{-1.0}$	$0.89^{+0.03}_{-0.03}$	$-0.71^{+0.18}_{-0.22}$	0.484 ‡	$0.91^{+0.14}_{-0.12}$	$20.2^{+2.3}_{-2.2}$	$2.15^{+0.23}_{-0.21}$	85^{+21}_{-21}	1.22 (330)

*, †, ‡ The notations and explanations follow table 2 except for the ionization parameter (ξ^{CSM}).

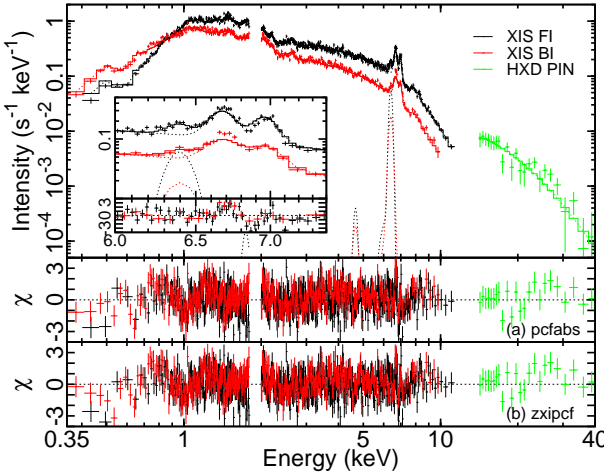


Fig. 7. Background-subtracted time-averaged spectra with the best-fit models. The symbols follow figure 4. Each spectral components are represented by dotted lines. The two residuals are for the fitting with partial coverage by (a) neutral matter and (b) ionized matter for the additional absorption. The former model is used for the uppermost panel.

best-fit parameters in the circumstellar absorption models. A significant decrease of the covering fraction (C^{CSM}) is seen in phase 2 in both models. A hint of the change in the hydrogen column density ($N_{\text{H}}^{\text{CSM}}$) is also seen in both models. The ionization parameter (ξ^{CSM}) in the ionized absorber model remains constant among the three phases. The spectral change in phase 2 is likely caused mainly by the change in the covering fraction.

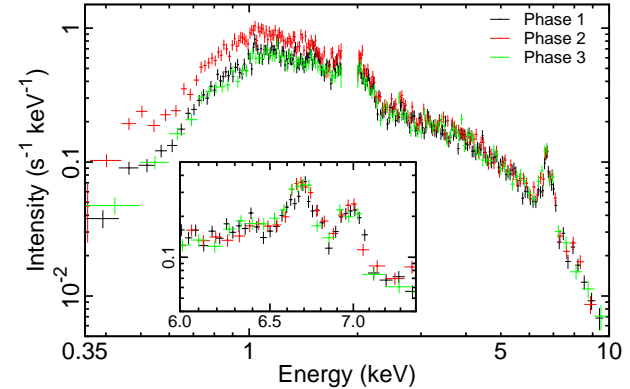


Fig. 8. Background-subtracted BI spectra in the three phases (figure 2) shown with different colors. The inset is an enlarged view for the Fe K α complex lines using FI spectra.

5. Discussion

5.1. Suzaku Confirmation and Expansion of ASCA Results

Z Cam was observed twice with ASCA in a transition phase and an outburst phase (Baskill et al. 2001). Our Suzaku observation was the second to be made in the X-ray during the transition phase of the object. Our result confirm and expand the results presented in the preceding work, which we briefly summarize here. Baskill et al. (2001) clearly showed the presence of the circumstellar absorption, which is larger than the interstellar absorption by two orders in the both the transition and outburst phases. The presence of such a large circumstellar absorp-

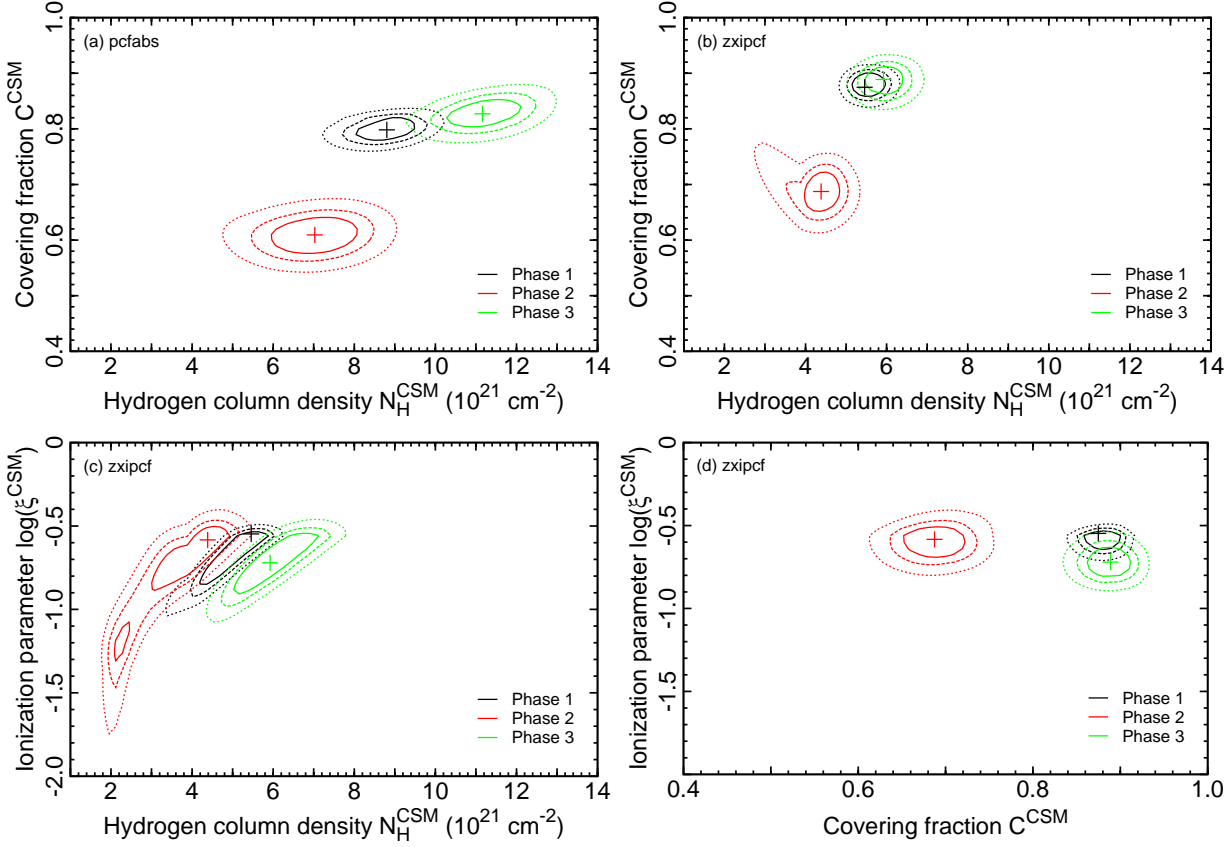


Fig. 9. Contour plot for the best-fit parameters in the circumstellar absorption model. (a) Partial absorption by neutral matter with the hydrogen column density (N_H^{CSM}) versus the covering fraction (C^{CSM}). (b) Partial absorption by ionized matter with N_H^{CSM} versus C^{CSM} , (c) with N_H^{CSM} versus the ionization parameter (ξ^{CSM}), and (d) with C^{CSM} versus ξ^{CSM} . Each color represents parameters in each phase. The solid, dashed, and dotted curves indicate 1, 2, and 3σ statistical confidence limits, respectively. The crosses indicate the best-fit values.

tion was confirmed by our observation (tables 2 and 3). Baskill et al. (2001) argued that the circumstellar absorption was ionized, but our data were explained equally well by partially covering neutral material.

Upon the confirmation of the previous ASCA findings, we further presented some new results, making use of the improved low-energy response and a wider band coverage of Suzaku. First, we found that the circumstellar absorption exhibits a time variation (figures 8 and 9). The variation is characterized by a decreased spectral hardness during a ~ 20 ks interval during our observation, which is mostly attributable to the change in the covering fraction. The variation is not associated with the orbital period of the system. We also detected reprocessed emission of the Fe fluorescence and the Compton scattering and constrained the plasma temperature and reflection geometry.

5.2. Timing of the Suzaku Observation

Our X-ray observation was made at the beginning of an optical outburst (figure 1). The rapid rise and slow decay of the optical light curve suggest that this outburst was an outside-in outburst (e.g., Lasota 2001), in which the heat wave propagates from the outer part of the accretion disk to the inner part. However, the X-ray characteristics

are those typical of the quiescent phase in the following three points.

First, in the Suzaku observation, the observed emission was quite hard with a 2–10 keV luminosity at 163 pc (table 1) of $8.5_{-0.1}^{+0.1} \times 10^{31}$ erg s $^{-1}$. The luminosity is quite similar to the EXOSAT measurement made at quiescence (Mukai & Shiokawa 1993) and is larger by 32 times than the ASCA measurement made at an optical and presumably X-ray outburst phase (Baskill et al. 2001). Here, we used the `pimms` tool⁴ for the flux conversion. In the dichotomy of enhanced and suppressed hard X-ray emission in the quiescent and outburst phases, respectively, the observed hardness and luminosity indicate that the Suzaku observation was made during the X-ray quiescent phase.

Second, with the observed X-ray data, we can estimate the accretion rate from the inner part of the disk to the WD surface (\dot{M}_{BL}). Assuming that an in-falling particle releases an energy of $(5/2)kT_{max}$, in which kT_{max} is the maximum plasma temperature of the boundary layer, the bolometric luminosity of the boundary layer is described as $L_{BL} = (5\dot{M}_{BL}kT_{max})/(2\mu m_H)$, where μ is the mean molecular weight (typically ~ 0.6) and m_H is the

⁴ See <http://heasarc.gsfc.nasa.gov/docs/software/tools/pimms.html> for details.

mass of hydrogen (Fabian 1994; Pandel et al. 2003). By substituting L_{BL} and kT_{max} with the observed values, we found that $\dot{M}_{\text{BL}} \sim 3 \times 10^{-11} M_{\odot} \text{ yr}^{-1}$, which is comparable to the typical value during the quiescence of DNe (Pringle & Savonije 1979; Pandel et al. 2003), but is much smaller than the value required for triggering outbursts ($\sim 10^{-9} M_{\odot} \text{ yr}^{-1}$: Osaki 1996; Lasota 2001).

Third, we derived a constraint of the reflection geometry from the spectral fitting using the hard X-ray emission above 20 keV and the Fe K fluorescent line (Ishida et al. 2009). Assuming that the WD surface contributes most as the reflector to reprocess the X-rays from the plasma, the solid angle subtended by the reflector ($\Omega/2\pi$) converts to the scale height (h) of the X-ray plasma from the WD surface (figure 5). Using the observed value $\Omega/2\pi = 0.484$ (tables 2 and 3), $h \sim 0.17R_{\text{WD}} = 9.7 \times 10^7 \text{ cm}$ (table 1), which is in line with the boundary layer being the source of the X-ray emission as in other DNe in the quiescent phase (Mukai et al. 1997; Ishida et al. 2009).

We thus conclude that our observation was made between the start of the state change in the outer part of the disk and the arrival of the heat wave to the inner part of the disk, in which optical outburst and X-ray quiescence co-exist. Such a transition phase is expected to last for ~ 1 day, which is the time for the heating front to traverse the disk (Lin et al. 1985). In fact, some X-ray observations were made in such a transition phase of DNe (e.g., Wheatley et al. 2003), including one of the two ASCA observations of Z Cam (Baskill et al. 2001). The entire Suzaku observation was within this transition phase as we see no signs of spectral change except for the change in the circumstellar absorption (§ 4.3.3 and § 4.4), but the last part of the ASCA observation was in the optical outburst phase as the X-ray luminosity declined in the last part of the observation with no change of spectral hardness. It suggests that the phase for an outburst of our Suzaku observation was preceded that of the ASCA observation.

5.3. Cause for the Circumstellar Absorption

We speculate the cause for the circumstellar absorption and its time variation. Two possible agents for the absorption are (i) disk wind and (ii) geometrically flaring disk. Both models can explain the observed extinction feature modeled by a partially-covering neutral or ionized absorption. In the wind model, the ionized partial absorption is expected to intervene in the line of sight with the covering fraction possibly representing the degree of porosity of the wind. In the flaring disk model, a part of the swollen disk is expected to cause a partial coverage either by neutral or ionized matter. The two models cannot be distinguished from our spectral results alone. However, we also found a time-variation of the circumstellar absorption, which is not associated with the orbital period. We would naturally expect the variation associated with the orbital period in the flaring disk interpretation, thus we favor the disk wind interpretation for the cause of the circumstellar absorption. Figure 5 shows a schematic view, in which the disk wind is triggered by the propagation of

the heat wave and causes a partial covering in the line of sight X-rays from the plasma localized in the boundary layer.

What is perplexing is that the time variation of the circumstellar absorption is not a monotonic increase and eventual saturation of the absorption column, which would be naïvely expected in the disk wind interpretation. The variation that we saw might be due to the change in the degree of porosity of the relatively stable wind, rather than the change in strength of the wind. A longer coverage of an outburst phase as well as the coverage of other phases far from the outburst and transition phases with the same data quality will help us to test our ideas.

The mechanism to launch disk wind is not well understood yet. If the absorption seen in our observation is caused by the wind, we argue that X-ray radiation pressure does not play an important role at least in the X-ray quiescent phase. First, the increase of the additional absorption in phase 2 does not accompany any changes in the intrinsic X-ray emission properties. Second, the X-ray radiation energy absorbed by the additional absorber can be derived as a difference between the additional-absorption corrected and uncorrected luminosity in the 0.35–10 keV band. The value $\sim 3 \times 10^{31} \text{ erg s}^{-1}$ is smaller than the wind mechanical energy of $\sim 8 \times 10^{32} \text{ erg s}^{-1}$ by more than an order with a mass loss rate of $\geq 2.4 \times 10^{-9} M_{\odot} \text{ yr}^{-1}$ (Robinson 1973) and a mean wind velocity of 1000 km s^{-1} (e.g., Warner 1995).

6. Summary

We conducted a Suzaku X-ray observation of the dwarf nova Z Cam at the onset of an optical outburst by chance. The X-ray spectral characteristics, however, suggest that the source was in the X-ray quiescent phase. This implies that our observation was made at the time when the heat wave had not reached to the inner part of the accretion disk in the development of the outburst, during which optical outburst and X-ray quiescent phases co-exist.

The X-ray spectrum shows clear evidence of an extra absorption upon the interstellar absorption, as was presented in the previous work. We found that (i) the extra absorption was modeled successfully by partial coverage either by neutral or ionized matter, (ii) the absorption shows a time variation with a time scale of $\sim 20 \text{ ks}$, (iii) the variation is mostly attributable to the change in the covering fraction, and (iv) the variation is not associated with the orbital period of the system. From these findings, we argued that the circumstellar absorption can be either by disk wind or geometrically flaring disk that intervene in the line of sight of the X-rays located in the boundary layer between the WD surface and the disk.

The authors acknowledge the referee, Knox S. Long, for improving the paper. The authors appreciate Dai Takei for his help in Suzaku data analysis. K.S. is financially supported by the Japan Society for the Promotion of Science. We acknowledge the variable star observations from the AAVSO International Database con-

tributed by observers worldwide. This research made use of data obtained from Data ARchives and Transmission System (DARTS), provided by Center for Science-satellite Operation and Data Archives (C-SODA) at ISAS/JAXA.

References

Anders, E., & Grevesse, N. 1989, *Geochim. Cosmochim. Acta*, 53, 197

Anderson, N. 1988, *ApJ*, 325, 266

Arnaud, K. A. 1996, in *ASP Conf. Ser.* 101, *Astronomical Data Analysis Software and Systems V*, ed. G. H. Jacoby, & J. Barnes, (San Francisco: ASP), 17

Baskill, D. S., Wheatley, P. J., & Osborne, J. P. 2001, *MNRAS*, 328, 71

Baskill, D. S., Wheatley, P. J., & Osborne, J. P. 2005, *MNRAS*, 357, 626

Bautista, M. A., & Kallman, T. R. 2001, *ApJS*, 134, 139

Bird, A. J., et al. 2010, *ApJS*, 186, 1

Boirin, L., & Parmar, A. N. 2003, *A&A*, 407, 1079

Boldt, E. 1987, *Phys. Rep.*, 146, 215

Córdova, F. A., & Mason, K. O. 1982, *ApJ*, 260, 716

Cusumano, G., et al. 2010, *A&A*, 524, A64

Done, C., & Osborne, J. P. 1997, *MNRAS*, 288, 649

Elvis, M. 2006, *Mem. Soc. Astron. Italiana*, 77, 573

Fabian, A. C. 1994, *ARA&A*, 32, 277

Fabian, A. C. 2010, in *IAU Symp. 267, Co-evolution of Central Black Holes and Galaxies*, ed. B. Peterson, R. Somerville, & T. Storchi-Bergmann (Cambridge: Cambridge University Press), 341

Feldmeier, A., & Shlosman, I. 1999, *ApJ*, 526, 344

Fukazawa, Y., et al. 2009, *PASJ*, 61, S17

George, I. M., & Fabian, A. C. 1991, *MNRAS*, 249, 352

Hartley, L. E., Long, K. S., Froning, C. S., & Drew, J. E. 2005, *ApJ*, 623, 425

Hellier, C. 2001, *Cataclysmic variable stars: how and why they vary* (Berlin: Springer-Verlag)

Ishida, M., Okada, S., Hayashi, T., Nakamura, R., Terada, Y., Mukai, K., & Hamaguchi, K. 2009, *PASJ*, 61, S77

Ishisaki, Y., et al. 2007, *PASJ*, 59, S113

Kaastra, J. S. 1992, *An X-Ray Spectral Code for Optically Thin Plasmas* (Internal SRON-Leiden Report, updated version 2.0)

Klare, G., Krautter, J., Wolf, B., Stahl, O., Vogt, N., Wargau, W., & Rahe, J. 1982, *A&A*, 113, 76

Knigge, C., Woods, J. A., & Drew, J. E. 1995, *MNRAS*, 273, 225

Knigge, C., Long, K. S., Blair, W. P., & Wade, R. A. 1997, *ApJ*, 476, 291

Kokubun, M., et al. 2007, *PASJ*, 59, S53

Koyama, K., et al. 2007, *PASJ*, 59, S23

Kubota, A., et al. 2007, *PASJ*, 59, S185

Lasota, J.-P. 2001, *New Astron. Rev.*, 45, 449

Liedahl, D. A., Osterheld, A. L., & Goldstein, W. H. 1995, *ApJ*, 438, L115

Lin, D. N. C., Papaloizou, J., & Faulkner, J. 1985, *MNRAS*, 212, 105

Long, K. S., & Knigge, C. 2002, 579, 725

Magdziarz, P., & Zdziarski, A. A. 1995, *MNRAS*, 273, 837

Mauche, C. W., Raymond, J. C., & Córdova, F. A. 1988, *ApJ*, 335, 829

Mewe, R., Gronenschild, E. H. B. M., & van den Oord, G. H. J. 1985, *A&AS*, 62, 197

Mewe, R., Lemen, J. R., & van den Oord, G. H. J. 1986, *A&AS*, 65, 511

Mitsuda, K., et al. 2007, *PASJ*, 59, S1

Mukai, K., & Shiokawa, K. 1993, *ApJ*, 418, 863

Mukai, K., Wood, J. H., Naylor, T., Schlegel, E. M., & Swank, J. H. 1997, *ApJ*, 475, 812

Mukai, K., Zietsman, E., & Still, M. 2009, *ApJ*, 707, 652

Oppenheimer, B. D., Kenyon, S. J., & Mattei, J. A. 1998, *AJ*, 155, 1175

Osaki, Y. 1996, *PASP*, 108, 39

Pandel, D., Córdova, F. A., & Howell, S. B. 2003, *MNRAS*, 346, 1231

Pringle, J. E., & Savonije, G. J. 1979, *MNRAS*, 187, 777

Ramsay, G., et al. 2001, *A&A*, 365, L294

Ritter, H., & Kolb, U. 2003, *A&A*, 404, 301

Robinson, E. L. 1973, *ApJ*, 186, 347

Serlemitsos, P. J., et al. 2007, *PASJ*, 59, S9

Shafter, A. W. 1983, *Ph.D thesis, UCLA*

Shlosman, I., & Vitello, P. 1993, *ApJ*, 409, 372

Smak, J. 1984, *PASP*, 96, 5

Szkody, P., & Mateo, M. 1986, *ApJ*, 301, 286

Takahashi, T., et al. 2007, *PASJ*, 59, S35

Thorstensen, J. R., & Ringwald, F. A. 1995, *Information Bulletin on Variable Stars*, 4249, 1

Thorstensen, J. R. 2003, *AJ*, 126, 3017

Tombesi, F., Sambruna, R. M., Reeves, J. N., Braito, V., Ballo, L., Gofford, J., Cappi, M., & Mushotzky, R. F. 2010, *ApJ*, 719, 700

Ueda, Y., Asai, K., Yamaoka, K., Dotani, T., & Inoue, H. 2001, *ApJ*, 556, L87

Verner, D. A., Ferland, G. J., Korista, K. T., & Yakovley, D. G. 1996, *ApJ*, 465, 487

Warner, B. 1995, *Cataclysmic variable stars* (Cambridge: Cambridge University Press)

Wheatley, P. J., van Teeseling, A., Watson, M. G., Verbunt, F., & Pfeffermann, P. 1996, *MNRAS*, 283, 101

Wheatley, P. J., Mauche, C. W., & Mattei, J. A. 2003, *MNRAS*, 345, 49

Wilms, J., Allen, A., & McCray, R. 2000, *ApJ*, 542, 914

Yamada, S., et al. 2011, *PASJ*, 63, S645